AIAA JOURNAL
Vol. 34, No. 7, July 1996

Unsteady Aerodynamics Associated with a Horizontal-Axis Wind Turbine

Stephen A. Huyer,[*] David Simms,[†] and Michael C. Robinson[‡]
National Renewable Energy Laboratory, Golden, Colorado 80401-3393

The wind turbine industry is currently facing many difficulties constructing efficient wind turbine machines caused by the inability to adequately predict structural loading and power output. Available evidence from wind turbines in a field environment suggests that formation of complex unsteady separated flowfields may be responsible for many aspects of wind turbine component failure. To examine this possibility in more detail, the Combined Experiment was developed. A full-scale wind turbine was constructed and operated in a field environment. The environment chosen was subject to wide variations in wind speed and direction and subsequently generated an extensive set of data for a variety of inflow test conditions. A single wind turbine blade was instrumented with pressure transducers and strain gauges with several data sets collected across a wide spectrum of typical and limiting wind turbine operating conditions. Surface pressure data taken at various spanwise locations along the blade demonstrated highly transient and spatially complex aerodynamic behavior for even the most basic operating conditions. Integrated normal force coefficient data showed enhanced lift values significantly beyond that predicted from steady-state two-dimensional wind-tunnel test data. Surface pressure data and integrated moment coefficient data suggested formation of coherent vortices consistent with the dynamic stall process observed in wind-tunnel tests for pitching wings. The unsteady, three-dimensional aerodynamic behavior for this wind turbine was then discussed and summarized.

Nomenclature

C_n = normal force coefficient
C_p = pressure coefficient, $P - P_\infty/q$
c = blade chord, m
K = reduced frequency parameter, $(\pi f c/V_{\mathrm{tot}})$
P = measure pressure, N/m^2
P_∞ = atmospheric pressure, N/m^2
q = instantaneous local dynamic pressure, $\frac{1}{2}\rho V_{\mathrm{tot}}^2$, N/m^2
q_0 = constant dynamic pressure, $\frac{1}{2}\rho(Vw^2 + Vr^2)$, N/m^2
R = blade radius or full semispan, 5.05 m
Re = Reynolds number, $cV_{\mathrm{tot}}/\upsilon$
r = local blade radius or span location, m
V_c = crossflow velocity component to disk, m/s
V_n = normal velocity component to rotor disk, m/s
V_r = local radial velocity, $r\omega$, m/s
V_s = spanwise velocity component, m/s
V_{tot} = total velocity (vector sum), m/s
V_w = local wind velocity, m/s
α = local blade angle of attack, deg
α^+ = effective nondimensional pitch rate $(\alpha * c/V_{\mathrm{tot}})$
α^* = effective pitch rate, rad/s
β = blade pitch angle, deg
γ = yaw (yaw angle-wind direction), deg
ρ = air density, kg/m^3
υ = coefficient of kinematic viscosity, m^2/s
ϕ = angle of total velocity vector relative to disk, deg
ψ = azimuth angle, deg
ω = radial frequency, $2\pi f$

Introduction

THE wind turbine industry is currently facing many difficulties constructing efficient and predictable wind turbine machines.[1–12] Power output and structural loads have been inadequately predicted, leading to the failure of power generators, gearboxes, and even turbine blades. This in turn increases operating and maintenance costs, making it difficult for the wind industry to compete with other established nonrenewable energy sources such as coal, oil, and gas. A 20- to 30-year wind turbine life span is necessary if wind power is to compete effectively with nonrenewable energy power sources. Because the corresponding loading and power output is caused by aerodynamic forces, the underlying fluid dynamics must be well understood to accurately determine structural and power requirements.

Steady-state, two-dimensional wind-tunnel data are generally used to estimate aerodynamic loads on wind turbine blades. The aerodynamic loading is then used to estimate structural loading and power output. According to Butterfield et al.,[5] Hansen and Butterfield,[6] and Huyer,[7] these methods consistently underpredict the actual loading and power output measured in the field. Two possible causes of the observed enhanced loading are unsteady and three-dimensional aerodynamic effects. There are currently no experimental data to determine the possible magnitude of these effects. The need for concrete experimental evidence provided the impetus for the Combined Experiment, designed to measure aerodynamic loads acting on a horizontal-axis wind turbine (HAWT) blade in a field environment. Surface pressure data were used to determine aerodynamic loading. Several pressure transducers and a high sampling rate allowed for exceptional spatial and temporal resolution of the unsteady flowfields elicited during normal wind turbine operation. These data were then compared with static results to approximate the influence of unsteady and three-dimensional aerodynamic effects.

Preliminary experimental evidence indicated that some underlying fluid dynamic phenomena could be attributed to dynamic stall. Vortex formation has been seen during the dynamic stall process in wind-tunnel tests for pitching and oscillating airfoils.[13–20] Although the blades on this particular wind turbine do not pitch or oscillate, yawing of the rotor disk caused by changes in wind direction, sudden wind gusts, or passage through the wake of the cylindrical support tower may produce geometrically similar motion histories. Wind-tunnel tests conducted by researchers at the University of Colorado[16–20] have shown that significant and highly

---

Received Oct. 14, 1993; revision received July 10, 1995; accepted for publication Aug. 25, 1995. This paper is declared a work of the U.S. Government and is not subject to copyright protection in the United States.

This article is dedicated to the fond memory of Professor Marvin Luttges.

[*] Postdoctoral Research Fellow, Applied Research Branch, National Wind Technology Center, 1617 Cole Boulevard; currently Mechanical Engineer, Hydrodynamics Branch, Naval Undersea Warfare Center, Newport, RI 02841.

[†] Senior Engineer, Applied Research Branch, National Wind Technology Center, 1617 Cole Boulevard.

[‡] Branch Manager, Applied Research Branch, National Wind Technology Center, 1617 Cole Boulevard.

transient loading occurs during the formation of these complex vortical flowfields. Two-dimensional tests conducted on pitching or oscillating airfoils have shown that lift coefficients as great as five times maximum static counterparts resulted during early formation of this vortex. As the vortex grew and was shed into the wake, significant decreases in lift and increases in pitching moment were observed. Tests on pitching rectangular wings[19] demonstrated similar lift overshoots, but vortex formation and shedding were then inherently more complex as the flow development process became three dimensional. Three-dimensional considerations are extremely important for a rotating wind turbine, because local wind velocity V_w and local angle attack α vary as a function of local blade radius r.

A collaborative research effort was established between the University of Colorado and the National Renewable Energy Laboratory to systematically categorize the local and global aerodynamic effects of a rotating wind turbine in a field environment. A physical understanding of the associated aerodynamics helps explain component failure to the wind turbine industry. This article presents some experimental data analyzed to date. Flow development histories based on these experimental data and previous wind-tunnel research are then proposed and discussed. Discussion of the unsteady aerodynamics produced by this wind turbine may also provide increased understanding of the unsteady flowfields generated by airplane or submarine propellers, helicopter rotors, and unsteady flows in compressors and ducted fans.

Methodology—Test Setup

A Grumman Wind Stream 33 downstream HAWT with 10.1-m rotor diameter and three-bladed hub was used in the Combined Experiment (Fig. 1) and was situated in the foothills outside Boulder, Colorado. The downstream design allowed for passive control in response to changes in wind direction. The turbine blades consisted of an S809 airfoil section with 45.7-cm chord and 4.3-m span, resulting in an aspect ratio of 9.4. The blade section begins at approximately 15% radius (0.7575 m) from the center of the hub and extends to 100% r (5.05 m). Spanwise locations are referenced from the center of the hub to the blade tip, and chordwise locations are referenced from the leading edge at a given spanwise location. To eliminate the complicated effects of wing geometry, a turbine blade of constant chord, zero twist, and zero taper was used. This allowed for data analysis for a given wind velocity, wind direction, and blade pitch angle only. Rotational velocity was held constant at 1.2 Hz (72 rpm) for all tests. Because rotational velocity was constant, instantaneous azimuth angle ψ was indicative of time relative to the rotation cycle. At $\psi = 0$ deg, the instrumented turbine blade is pointing straight up (at 12:00), and at 180 deg, the turbine blade is directly behind the cylindrical support tower. Also, the turbine blade rotates clockwise for an observer looking from behind the turbine into the wind. A vertical plane array consisting of 13 prop-vane anemometers was located one rotor diameter upstream of the turbine and was spaced to characterize the inflow to the turbine. These anemometers provide wind velocity and direction and are similar to those used to collect meteorological data. Wind direction was provided by an anemometer located at the center of the disk, and wind speed was available at 12 other locations. Wind speed was computed as an average of the eight prop-vanes located at 40% radius (referenced from the center of the hub). Frequency response of these anemometers was approximately 2 Hz and was sufficient to characterize atmospheric changes on wind velocity and direction. More information regarding the details of the test setup may be found in Butterfield[1] and Butterfield et al.[2,3]

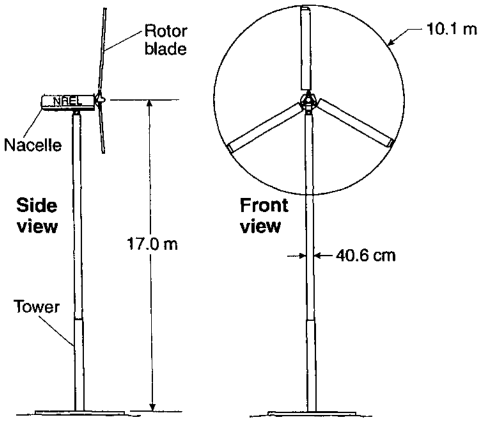

Fig. 1 Grumman Wind Stream 33 downwind HAWT.

Instrumentation

Upper and lower surface pressure measurements were made at different chordwise and spanwise locations. Four 32-tap ESP-32 pressure transducers were installed inside the test blade near the chordwise distributed taps and were close coupled to the blade surface. At 30, 47, 63, and 80 local semispan, 36 pressure taps, 1.0 mm in diameter, were aligned along the chord. Pressure transducers were also distributed in approximately 6% span increments at 4 and 36% chord to provide spanwise pressure distributions. Pressure data P were collected at a sample rate of 520.8 Hz and alias filtered at 100 Hz. Fast Fourier transform analysis of various pressure data sets clearly demonstrated that the spectral content of the pressure fluctuations remained below 50 Hz (see Ref. 8). Atmospheric pressure P_∞ was then subtracted and normalized by instantaneous local dynamic pressure q to compute the local pressure coefficients. Integrating the pressure data provided normal and tangential force coefficient data. Results of the uncertainty analysis for selected measured channels are presented in Table 1. The total estimated uncertainty values listed are expressed in engineering units and represent random and bias error components. The uncertainty is also expressed in terms of percent full-scale error. Calibration procedures were established to ensure that all recorded data values were within the stated error limits. Detailed measurement uncertainty estimates for all 239 measured channels can be found in Ref. 8. Error analysis and calibration procedures specific to wind turbine field testing are described in Ref. 9.

The four 32-channel scanning pressure transducers in the turbine blade required frequent calibration to maintain accuracy. These transducers tend to zero drift because ambient conditions vary. To ensure accuracy, all 128 pressure channels were calibrated before and after each 10-min data event. A custom-built pressure system controller mounted on the turbine hub was used to automate the calibration process. Calibrations were invoked in the field by remote control while the turbine was in motion. This system is described in detail in Refs. 10 and 11. It uses a motorized syringe to provide positive and negative ramping pressure to all scanning transducer ports simultaneously and to a precision differential reference pressure transducer. Calibration coefficients were derived by performing a least-squared regression on data from each of the 128 pressure channels referenced to the precision calibration transducer signal. To quantify the effect of measurement drift on bias error, resulting calibration coefficients from before and after each 10-min data event were compared to determine whether each channel remained within the required error limits during the event. If errors exceeded limits for any channel, the entire data event was discarded. Also shown in Table 1 are minimum dynamic pressure values for the four span locations. These correspond to zero turbine power production at a rotational velocity of 1.2 Hz and wind velocity of 7.6 m/s. Measurement uncertainties are less than 15% of the minimum dynamic pressure.

Table 1 Uncertainty analysis results for selected measured channels

Measurement	Units	Full-scale measurement range	Total estimated uncertainty	Full-scale error,%	Minimum dynamic pressure
Pressures at 30% span	N/m^2	±2970	±12	0.2	90
Pressures at 47% span	N/m^2	±2970	±18	0.3	190
Pressures at 63% span	N/m^2	±8274	±33	0.2	310
Pressures at 80% span	N/m^2	±8274	±50	0.3	480
Wind velocity	m/s	0–37	±0.5	1.4	——
Blade pitch angle	deg	−10–71	±1.0	1.2	——
Blade azimuth angle	deg	0–360	±1.0	2.8	——
Barometric pressure	mb	800–1100	±3.0	1.0	——

Various procedures were used to ensure that the nonpressure channels maintained the required accuracy levels. The preferred method of calibrating channels in the field was to use an end-to-end procedure where a known response was applied at the transducer, thus enabling the full system measurement path to be calibrated. For some channels, it was impossible to perform full-path calibrations in situ. For example, anemometers are typically calibrated with known wind velocities in a wind tunnel. In these cases, a two-part calibration was used. The first part relies on factory-supplied transducer calibration results. The second part is an electronics cal, where precision reference voltages are inserted in place of the transducer signal, and a system electronics path is calibrated separately. The frequency of these types of calibrations depends on transducer and measurement system specifications and varies with use and application. Further information on the data measurement system and calibration procedures can be found in Refs. 8–11.

Analytical Procedure

Typical data sets consisted of 239 channels of data sampled at 520.8 Hz over 5 min. This generated enormous amounts of data, with each data set consisting of approximately 150 Mbytes of digital data. Analysis of entire data sets was impractical, and so specific subsets, which conformed to desired input criterion of wind velocity and wind direction, were analyzed. For time series data, an algorithm was developed that extracted continuous strings of those data. For analytic simplicity and consistency, complete data cycles where ψ varied from 0 to 360 deg were examined to determine temporal characteristics of the dependent variables.

Angle-of-attack α and dynamic pressure q data were vital for pressure and force data analysis. A basic analytical model of q and α was constructed on the basis of the geometric setup of the wind turbine relative to the wind and is shown in Fig. 2. For nonzero yaw γ, local wind velocity was reduced to normal and crossflow components relative to the rotor disk:

$$V_n = V_w(1 - a)\cos\gamma \tag{1}$$

$$V_c = -V_w \sin\gamma \tag{2}$$

where a is a factor that includes deceleration of the wind caused by wind turbine operation.

The tangential velocity vector is then modified because of crossflow as a function of blade azimuth angle ψ:

$$V_t = V_r + V_c \cos\psi \tag{3}$$

$$V_s = V_c \sin\psi \tag{4}$$

and so

$$V_{\text{tot}} = \left(V_n^2 + V_t^2 + V_s^2\right)^{\frac{1}{2}} \tag{5}$$

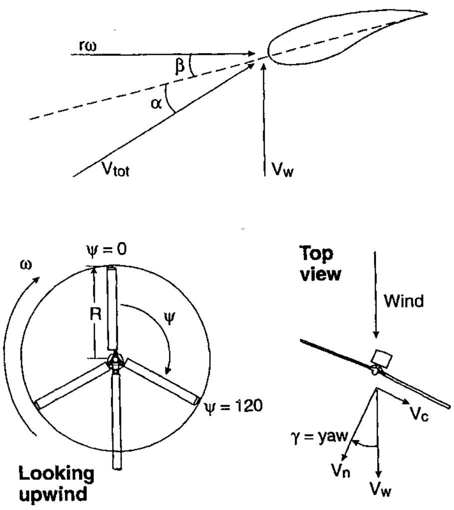

Fig. 2 Blade angle-of-attack geometry.

Local dynamic pressure is then defined as

$$q = \tfrac{1}{2}\rho V_{\text{tot}}^2 \tag{6}$$

velocity vector angle as

$$\phi = a\tan(V_n / V_t) \tag{7}$$

and local angle of attack relative to local blade chord line as

$$\alpha = \phi - \beta \tag{8}$$

Finally, a simple model of the velocity deficit in the wake of the tower was constructed. A cosine function was used to estimate the mean velocity profile with a maximum deficit of 30% of the total wind velocity and 2-diameter wake width.

The data presented in this report summarize the effects of increased wind velocity and γ angle on the surface pressure distributions for a rotating wind turbine. Cycle averaged data, consisting of five data cycles with similar wind velocity and yaw angle criteria that were ensemble averaged, are presented. In general, individual data cycles were extracted from different points in the test run and were not sequential. They do, however, demonstrate the repeatable nature of the flow structures that form. Single data cycles are also presented to demonstrate the effects of defined vortex structures. Average wind velocities of 7.7, 14.7, 18.7, and 23 m/s were examined for a 0-deg γ, and 30, −30, 15, and −15-deg γ cases were examined for a constant wind velocity of 15 m/s. Reynolds numbers in this experiment were on the order of 5×10^5 but varied along the blade span because of differing rotational velocities. Surface pressure distributions were plotted as a function of ψ representing a time series of data at 30, 47, 63, and 80% spanwise locations. Surface pressure data were normalized by freestream dynamic pressure q_0, which was calculated based on rotational velocity and wind velocity alone. Integrated normal force coefficients were plotted as a function of ψ. In addition, normal force data were plotted as a function of α to allow for direct comparisons (based on the computed model) with steady-state wind-tunnel data. These data were normalized by a computed dynamic pressure model that incorporated the effects of γ and tower shadow. This was necessary because dynamic pressure is constant for wind-tunnel tests but varies over the rotation cycle due to crossflow for a yawed turbine.

Results: Steady-State Airfoil Performance

A cross section of the S809 airfoil section is shown in Fig. 3, drawn to scale. Actual airfoil coordinates were presented by Butterfield et al.[3,8] This airfoil has a maximum thickness of 21% at approximately 45% chord. The plot of the camber line is not drawn to scale. As can be seen, the curvature of the camber line transitions from positive to negative to positive. The camber is positive (concave down) from the leading edge to approximately 20% chord, it is negative from 20 to 60% chord and positive again from 81% c to the trailing edge. The S809 airfoil was designed specifically for wind turbine applications.

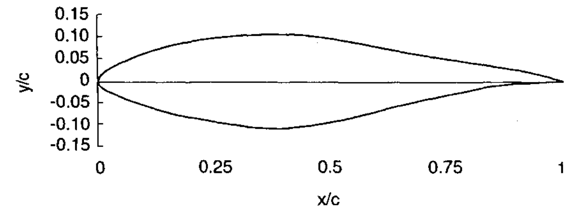

S809 airfoil

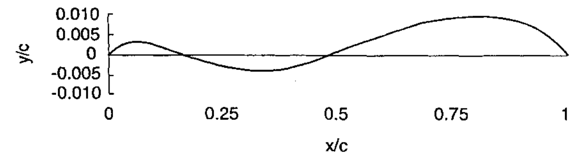

S809 camber line

Fig. 3 S809 airfoil section with camber line.

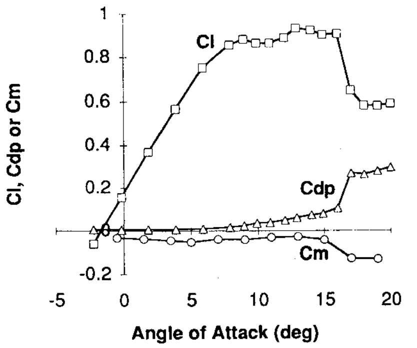

Fig. 4 Steady-state C_n, C_d, and C_n vs α from Butterfield et al.[8]: S809 airfoil, $Re = 5 \times 10^5$.

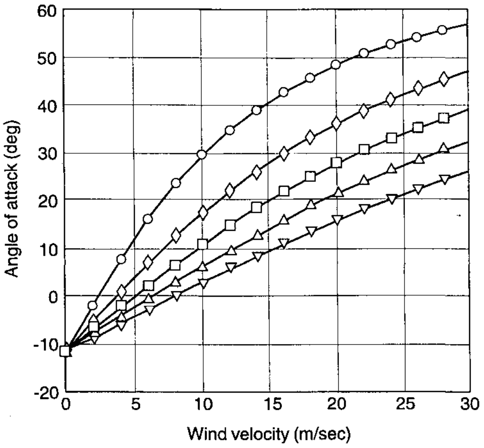

Fig. 5 Theoretical angle of attack vs wind velocity: -○-, 30% span; -◇-, 47% span; -□-, 63% span; -△-, 80% span; and -▽-, tip.

Figure 4 shows the aerodynamic performance measured in force coefficient data for the S809 airfoil section. These data were collected from wind-tunnel tests and more detailed results may be found in Butterfield et al.[3,8] The lift, drag, and moment coefficients plotted were derived directly from surface pressure data (i.e., no skin-friction effects) for a Reynolds number of 5×10^5. The positive camber effect near the leading edge results in nonzero lift at 0-deg angle of attack with $C_l = 0.18$. From $\alpha = -2$–8 deg, lift increases linearly. From $\alpha = 9$–15 deg, the lift does not increase appreciably and indeed decreases at $\alpha = 11$ deg. It is stressed, however, that the airfoil section is not yet stalled. This can be seen from the drag data and especially the moment coefficient data. Even though the lift curve slope is flat, there still is not a strong negative pitching moment. Although not shown, pressure data continued to show a strong leading-edge suction pressure peak. The airfoil section finally stalls at $\alpha = 16$ deg. Here, C_l decreases to 0.655, C_d increases to 0.271, and a strong negative pitching moment with $C_m = -0.13$ was observed. The aerodynamic characteristics of this particular airfoil section seem peculiar when compared with standard NACA 00 series airfoil sections. Recall, however, that these airfoil sections were designed specifically for wind turbine applications. Wind turbines generally must operate at or near static stall to achieve maximum efficiency. To lessen the impacts of cataclysmic stall on the blade, the airfoil section was designed to ease into stall. Although this may assist in reducing some undesirable unsteady effects, as will be seen later, the effects of unsteady flows, specifically dynamic stall, are tremendous.

Additional wind-tunnel tests were conducted for Reynolds numbers ranging from 3×10^5 to 6.5×10^5 to gauge possible effects of Reynolds number on airfoil stall sensitivity. These results were also presented in Butterfield et al.[3,8] The data demonstrated a slight reduction in static stall angle from 16 to 15.2 deg and 5% reduction in $C_{l\,\max}$ for $Re = 3 \times 10^5$. There was little appreciable change as the Reynolds number was increased from 5×10^5 to 6.5×10^5.

Figure 5 shows the computed geometric angle of attack variation as a function of wind speed at 30, 47, 63, and 80% span locations corresponding to the pressure port locations. As can be seen from this figure, even moderate wind speeds will result in significant blade angles of attack with much of the blade operating in the poststall regime for a constant wind velocity and zero yaw. As will be demonstrated later, fluctuations in wind velocity and wind direction result in significant angle-of-attack variations over a single blade rotation cycle, thereby producing significant unsteady aerodynamic effects.

Zero-Yaw Test Cases

Upper surface pressure distributions are plotted topologically in Fig. 6 at 47% span for zero γ and 14.7-m/s wind velocity. Five data cycles were ensemble averaged. Suction pressure was plotted along the chord as a function of instantaneous ψ. At $\psi = 0$ deg, the blade is at 12:00, and at $\psi = 180$ deg, the blade is at 6:00 and was located directly behind the tower. For $V_{ws} = 14.7$ m/s, local α was 27.4 deg. At 47% span, the pressure distribution showed a pronounced increase in leading-edge (LE) suction pressure at $\psi = 190$ deg, and a ridge in suction pressure that formed in the direction of increasing chord and ψ. This ridge appeared to persist to the trailing edge. During the remainder of the cycle, C_p values of approximately -1.0 were observed and were consistent with stalled flow conditions. Because of the high α, stalled flow conditions were expected throughout the entire rotation cycle, but the pressure distribution indicated flow reattachment as the blade passed through the tower wake.

Normal force coefficients were plotted as a function of ψ to demonstrate the global effects of increased wind velocity at 80% span (Fig. 7). Passage through the tower wake had significant effects on C_n values for each wind velocity and span location examined. For the low-speed test case (7.7 m/s and local $\alpha = 2$ deg), C_n values remained effectively constant until the blade passed through the tower wake. This could be seen by a significant decrease in normal force coefficient (C_n). Average C_n values appeared to be approximately 10% less than the static counterparts obtained during two-dimensional wind-tunnel tests.

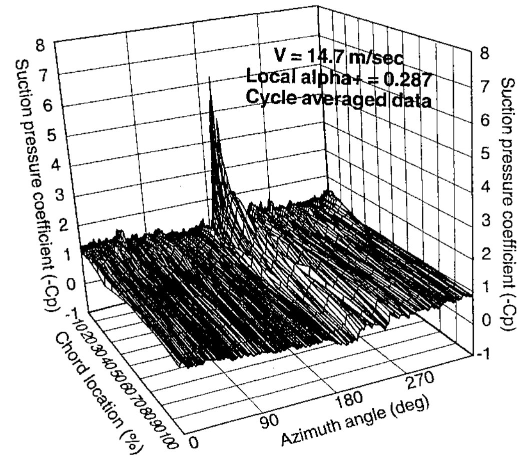

Fig. 6 Upper surface pressure distribution vs azimuth angle; $V_w = 14.7$ m/s, $\gamma = 0$ deg, and 47% span location.

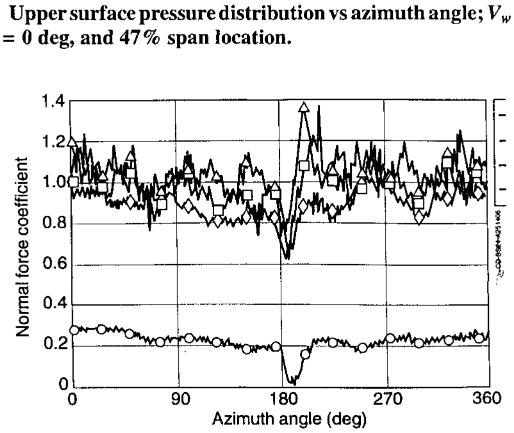

Fig. 7 Normal force coefficients vs azimuth angle; at 80% span for zero yaw test cases. Cycle averaged data. 0-deg yaw, 80% span: -○-, 7.7 m/s; -◇-, 14.7 m/s; -□-, 18.7 m/s; and -△-, 23 m/s.

As wind velocity was approximately doubled to 14.7 m/s (local $\alpha = 14$ deg), C_n increased to approximately 0.85. This was approximately 5% greater than static values for equivalent α. For the high wind speeds (18.7 and 23 m/s and local $\alpha = 20$ and 24 deg), C_n values increased further, and consistent lift enhancement was seen compared with static wind-tunnel values at all span locations. In addition, lift overshoots 40% greater than maximum static values were seen as the blade passed through and out of the tower wake. Geometrically, the blade should be stalled at 80% span. Significant lift enhancement and lift overshoots were seen, however.

Effect of Yaw

Effects of yaw error (referred to as γ) resulted in even more complex pressure distributions compared with the zero γ case. Although the turbine automatically oriented itself with respect to the wind, rapid variations in wind direction typically create large yaw errors until the machine reorients itself. For yawed data, the effect of passage through the tower wake as well as cyclic variation in q and α were superimposed, making it very difficult to predict the possible flowfields that were formed. Repeatable trends were found and will be summarized in this section.

Upper surface pressure distributions for the 30-deg γ case are shown in Figs. 8 and 9 for 30 and 63% spanwise locations. At 30% span, very large (-8.5) and transient LE suction pressure peaks were formed at approximately $\psi = 140$ and 180 deg. It is likely that the first peak was a result of passage through the tower wake. Because of the high γ, the blade would be passing through the wake at this point in the rotation cycle. The formation of the second peak was seen later and was significantly larger. The formation of a suction pressure ridge in the direction of increasing chord and ψ was also observed.

The pressure distribution at 63% span was significantly different. At $\psi = 165$ deg, a pronounced decrease in suction pressure (from -3.5 to -1.5) was seen as the blade passed through the tower wake.

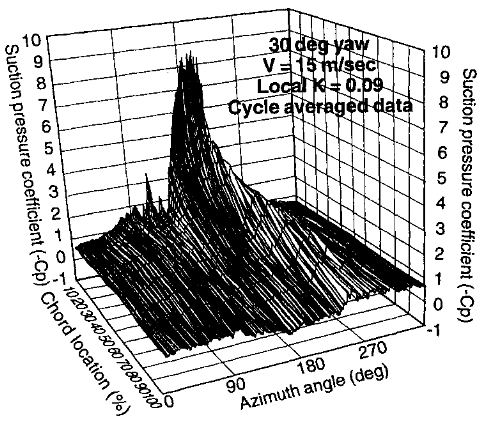

Fig. 8 Upper surface pressure distribution vs azimuth angle; V_w = 15 m/s, γ = 30 deg, and 30% span location.

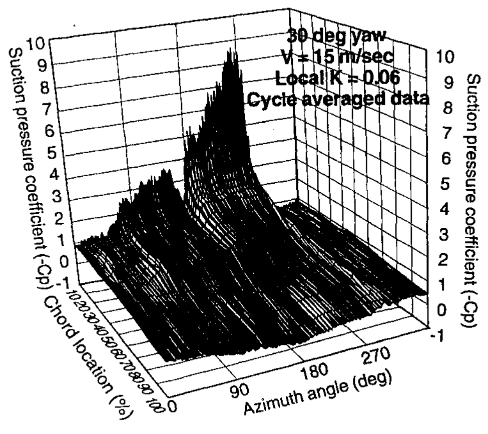

Fig. 9 Same as Fig. 8 except 63% span location.

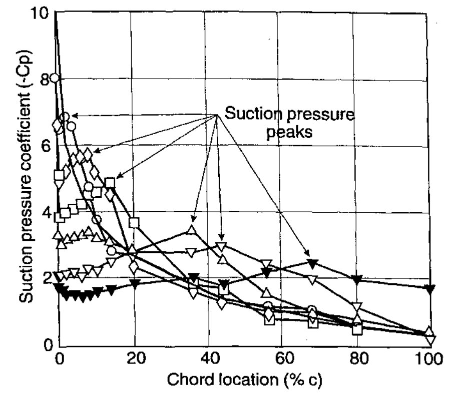

Fig. 10 Suction pressure coefficient vs chord location; V_w = 15 m/s, γ = 30 deg, and 30% span location. Single-cycle data. Chordwise pressure distributions taken at specific points in rotational cycle. Single cycle: ——, 186 deg; -○-, 192 deg; -◇-, 196 deg; -□-, 205 deg; -△-, 218 deg; -▽-, 227 deg; and -▼-, 245 deg.

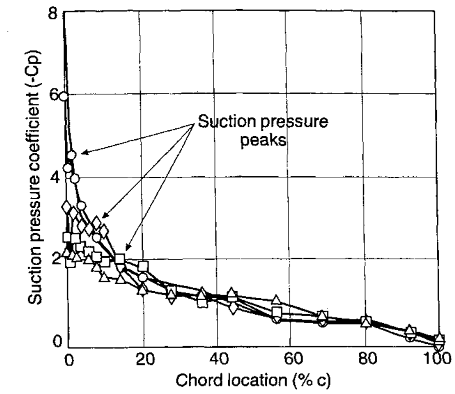

Fig. 11 Same as Fig. 10 except 63% span location; V_w = 15 m/s, γ = 30 deg, and 63% span. Single cycle: ——, 276 deg; -○-, 278 deg; -◇-, 281 deg; -□-, 284 deg; and -△-, 288 deg.

As the blade came out of the wake, a gradual increase in LE suction pressure was seen from $\psi = 180$ to 280 deg with a maximum value of -8.5. This gradual increase in LE suction pressure was immediately followed by a precipitous decrease to -1.0, and the blade section exhibited stalled flow conditions.

Although upper surface pressure distributions demonstrated highly transient behavior, conclusive evidence of vortex formation was desired. Chordwise pressure distributions were examined to highlight the formation of a suction pressure ridge seen in the three-dimensional pressure distributions. Since the pressure ridges were most obvious in the single cycle data, these data were examined to follow the suction pressure peaks as the rotational cycle advanced. Chordwise pressure distributions are shown in Figs. 10 and 11 at 30 and 63% span locations, respectively, for the 30-deg γ test case and 15-m/s wind velocity. Multiple plots are shown as the rotational cycle advanced, emphasizing the temporal displacement of the suction pressure ridge. A vortex produces a definite signature in a chordwise pressure distribution because it is defined as a region of low pressure.[17–19] If a vortex is present, a suction pressure peak in the chordwise pressure distribution would exist corresponding to the approximate location of the vortex. If no vortex was present, suction pressure would decrease as $1/c$ for cases of attached flow, similar to static two-dimensional wind-tunnel results.

At 30% span, the pressure distribution taken at $\psi = 186$ deg, the pressure appeared to decrease as $1/c$. Maximum LE suction pressure was observed at this point in the rotation cycle. At $\psi = 192$ deg, a suction peak of -6.84 was seen at 2% c. At $\psi = 196$ deg, the suction peak moved to 6% c, and at 205 deg, it moved to 14% c. Notice that as the pressure peak moves downstream, its magnitude diminished but the spatial region of low pressure increased. As the rotation cycle continued, the pressure peak moved downstream and was centered at 36% c for $\psi = 218$ deg, 44% c for $\psi = 227$ deg, and 68% c for $\psi = 245$ deg.

At 63% span, the only suction peaks observed were located upstream of 8% *c*. A small pressure peak was seen at 1% *c* for $\psi = 278$ deg and moved to 8% *c* for $\psi = 281$ deg. A small peak may be implied at 14% *c* for $\psi = 284$ deg, but no further peaks were observed downstream as the cycle advanced. The remaining chordwise pressure distributions were more indicative of stalled flow conditions. Although not shown, there was no evidence at 80% span of suction pressure peaks downstream of the LE at any time during the rotation cycle following the time where maximum LE suction pressure occurred.

Normal force coefficient was plotted as a function of ψ for the 30-deg γ case at the four different spanwise locations (Fig. 12). Normal force appeared to vary sinusoidally as a function of ψ. At 30% span, a clearly defined maxima in C_n was observed. At the remaining span locations, C_n maxima persisted over approximately a quarter of the rotation cycle. At 30% span, significant lift overshoots were seen with maximum C_n of 2.4 observed at $\psi = 225$ deg. At 47% span, maximum normal force values were seen between $\psi = 180$ and 225 deg with maximum C_n of 1.8 observed. At 63% span, maximum C_n were seen at $\psi = 225$ deg but equivalent C_n values of 1.4 were seen between $\psi = 190$ and 280 deg. At 80% span, maximum C_n values were observed between $\psi = 200$ and 290 deg with maximum values on the order of 1.1. At $\psi = 310$ deg, a significant decline in normal force was observed. At all span locations, maximum normal force values were greater than static counterparts with maximum values at 80% span approximately 30% greater than static counterparts.

Moment coefficient data were plotted in Fig. 13 as a function of ψ for $\gamma = 30$ deg at the four different spanwise locations. For all cases, the moment coefficient remains negative (pitch down). At 30% span, a moderate pitch down moment of −0.28 was observed at $\psi = 90$ deg. This is followed by a decrease in negative C_m with values under −0.1 from $\psi = 135$ to 180 deg. Here, C_m values are equivalent with steady-state results for attached flow (see Fig. 4). Pitch down moment then increases and reaches a maximum of −0.43 at $\psi = 240$ deg. At this time, C_n values at 30% span presented in the preceding figure had reached maximum values and were just beginning to decrease. Negative C_m values then decrease as the rotation cycle continues.

At 47% span, negative C_m values begin to increase just after $\psi = 180$ deg. At this point in the rotation cycle, C_m values are equivalent with steady-state attached flow data. Peak negative C_m of −0.26 was observed at $\psi = 263$ deg. Consistent with results observed at 30% span, the normal force coefficient data at this span location have already attained maximum values and just begin to exhibit the largest decrease. At 63% span, C_m data from $\psi = 0$ to 280 deg generally remain comparable to steady-state values seen for attached flow. At $\psi = 290$ deg, negative C_m values increase to −0.165. Again, this occurred just after normal force values began to decrease. At 80% span, C_m values are consistently remain below −0.1 with negative pitching moments equivalent with those observed for steady-state results for attached flow.

Angle of attack and *q* are plotted in Figs. 14 and 15, respectively. These graphs demonstrate the effective temporal motion histories for a yawed turbine with respect to the wind for the 30-deg γ case. Effects the tower wake are included. Angle-of-attack variations are greatest at 30% span and smallest at 80% span. At 30, 47, and 63% span, effective α ranged from pre- to poststatic stall, based on wind-tunnel data. At 80% span, maximum α were found to be comparable to static stall α. Temporal variations in q were found to be 180-deg out of phase compared with angle-of-attack variations. In addition, the largest variations in *q* occurred at 80% span with the relative amplitude decreasing at inboard spanwise locations.

Large cyclic variations in *q* associated with a yawed turbine were demonstrated in Fig. 15. For the present observations to be

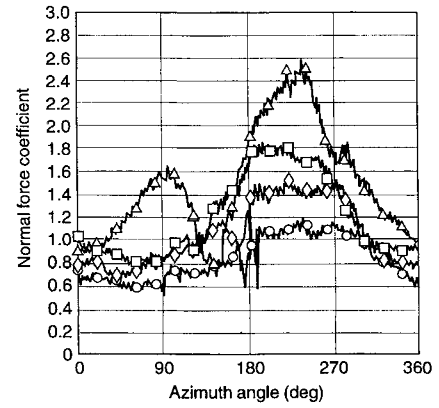

Fig. 12 Normal force coefficient vs azimuth angle for 30-deg yaw and V_w = 15 m/s at the four span locations examined. Cycle-averaged data. 30 deg yaw, V = 15.0 m/s: -○-, 80% span; -◇-, 63% span; -□-, 47% span; and -△-, 30% span.

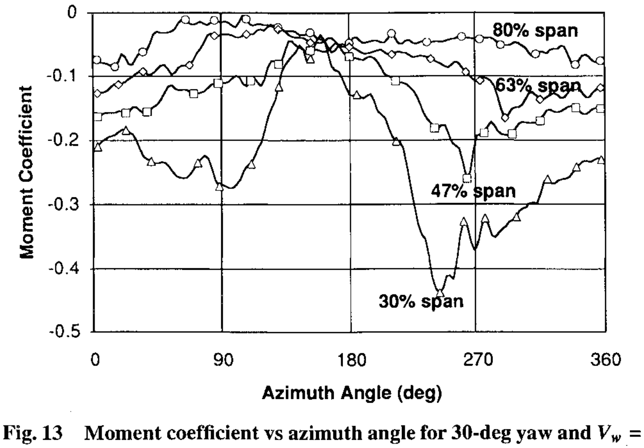

Fig. 13 Moment coefficient vs azimuth angle for 30-deg yaw and V_w = 15 m/s at the four span locations examined. Cycle-averaged data: 30-deg yaw and V = 15.0 m/s.

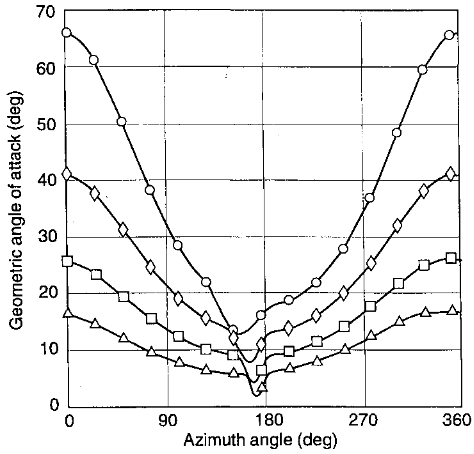

Fig. 14 Theoretical angle of attack vs azimuth angle at 30, 47, 63, and 80% span locations for the 30-deg yaw cases examined: -○-, 30% span; -◇-, 47% span; -□-, 63% span; and -△-, 80% span.

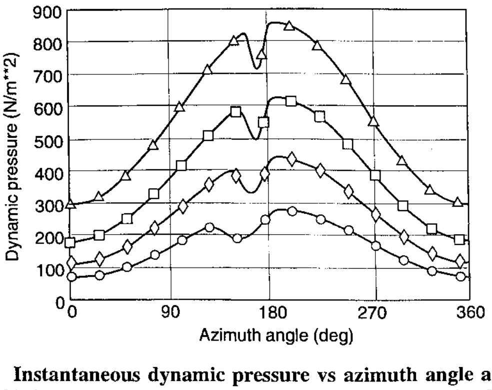

Fig. 15 Instantaneous dynamic pressure vs azimuth angle at 30, 47, 63, and 80% span locations for the 30-deg yaw cases examined. V = 15 m/sec, 30-deg yaw: -○-, 30% span; -◇-, 47% span; -□-, 63% span; and -△-, 80% span.

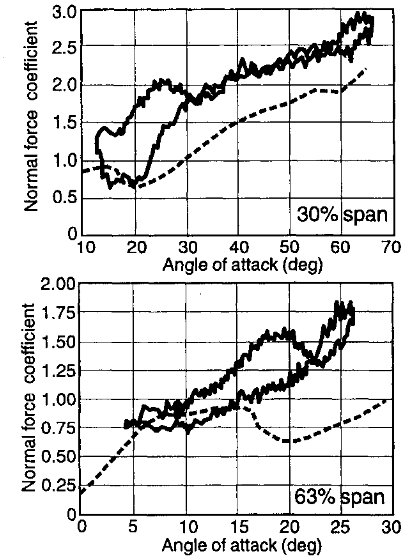

Fig. 16 Normal force coefficient vs angle of attack at 30 and 63% span locations; V_w = 15 m/s, γ = 30 deg, and cycle-averaged data. C_n normalized by instantaneous dynamic pressure q. 30-deg yaw, q corrected data.

consistent with wind-tunnel tests, C_n were nondimensionalized by q. These results may be seen in Fig. 16 for 30-deg γ at 30 and 63% span locations. Because constant dynamic pressure (q_0) was used in the wind-tunnel tests referenced earlier, it seemed reasonable to nondimensionalize the force coefficients by q to provide for fair comparisons. The C_n vs α curves shown in Fig. 16 for the 30-deg γ case were significantly different compared with nondimensionalization by q_0. At 30% span, a hysteresis loop was observed between $\alpha = 15$ and 30 deg with considerable lift enhancement twice that of static values observed. From 30 to 65 deg, little hysteresis was seen, although lift enhancement was still observed; however, the lift slope followed that of the static data with dynamic values offset by approximately 0.5. Finally, maximum C_n values were seen at maximum α.

At 63% span, the width of the hysteresis loop appeared to diminish, but lift enhancement was still observed and was as great as 75% over maximum static values. Minimal lift reduction was seen at the lower effective α for decreasing α. At each span location, maximum C_n values were observed at maximum α and were qualitatively consistent with wind-tunnel data provided for oscillating wings.[17–19]

Discussion

Experimental data were reduced with the goal of first extracting the most basic test cases; specifically, constant wind speed and selected yaw angles. By maintaining constant wind velocity with zero yaw, it was predicted that the aerodynamic behavior would be quasisteady with minor effects resulting from the cylindrical tower wake. This prediction proved to be incorrect. Pressure distributions demonstrated highly unsteady and three-dimensional behavior. Integrated normal force data showed that the magnitude of the forces could not be accurately and reliably predicted using steady-state wind-tunnel data. As the wind turbine was yawed with respect to the approaching wind, the problems associated with the unsteady and three-dimensional aerodynamics made it even more difficult to adequately predict the flowfield behavior associated with a HAWT. Even so, a great deal of the unsteady aerodynamic behavior was learned from the Combined Experiment and will be discussed here.

Wind Turbine Operating States

Steady-state analysis of the wind turbine aerodynamics greatly simplifies understanding of some of the more basic issues and is appropriate as long as the local blade angles remain below static stall. This is indeed the case over much of the blade for zero yaw operation and low wind speeds (i.e., below 10 m/s). The reader is referred to two sources to provide more detail. Spera[12] provides a good summary of some of the basic aerodynamics in two chapters in his book. Hansen and Butterfield[6] also discuss some of the steady-state aerodynamics based on experimental data, as well as some of the computational and analytical methods used in engineering design. Some of their findings are summarized in this section.

A wind turbine extracts energy from the Earth's atmosphere to produce power. This is accomplished by situating the turbine blades in some manner with the atmospheric disturbances (i.e., wind). Most HAWTs rotate at a constant angular velocity regardless of wind velocity. Power output is then directly related to the wind velocity. Except for excessively low wind speeds, there is sufficient energy to turn the blades and generate power. The turbine used in this experiment is referred to as a downwind turbine because the rotor disk is oriented downstream of the support tower. Downwind orientation allows the blades to deflect away from the tower as thrust loading increases. In addition, passive control is employed allowing the rotor disk to orient itself to changes in wind direction. Disadvantages of this design include interactions with the tower wake (as will be discussed later) and slow adjustment to rapid changes in wind direction.

Because the rotational velocity is constant, wind velocity and local blade velocity $r\varpi$ determine the effective angle of attack of the turbine blade relative to the wind. An increase in wind velocity results in an increase in local α along the blade. Conversely, an increase in local blade velocity results in a decrease in α, and so the local α decreases at outboard span locations. Variations in wind velocity caused by gusts will produce angle-of-attack fluctuations along the blade with the amplitude dependent on the magnitude of the wind velocity and the scale of the disturbance. There will also be variations in wind velocity caused by the presence of an upstream structure. In the current tests, the presence of the cylindrical support tower produces impulsive variations in α because of passage through the tower wake. Schlichting[21] summarizes some experimental data for flow about circular cylinders at these Reynolds numbers. On average, a velocity defect as great as 30% freestream values may be expected. In addition, the shape of the wake appears as a cosine function. Therefore, as the blade passes through the tower wake, it experiences a decrease in local wind velocity followed by an increase resulting in decreased, then increased α.

When the rotor disk becomes yawed with respect to the oncoming wind, an effective sinusoidal variation in α over the rotation cycle arises from the crossflow velocity component relative to the rotor disk. Depending on the position of the turbine blade in the rotation cycle, it may be heading into the crossflow (resulting in decreased effective α) or translating with the crossflow (resulting in increased effective α). The amplitude of the sinusoidal variation in α depends on the magnitude of the yaw angle, wind velocity for mean α, and blade rotation frequency for the oscillation frequency.

The analytic expressions for angle of attack shown in Eq. (8) and plotted in Fig. 14 for the case of $\gamma = 30$ deg are based on this formulation. Indeed, there are additional effects that were not accounted for in the analytical model that should be of second order. These effects include horizontal and vertical wind shear caused by the atmospheric boundary layer near the surface. For the test conditions presented in this article, maximum horizontal and vertical wind shear were found to be below 5% of the maximum wind velocity. In other tests not presented, however, horizontal and vertical wind shear can be significant (i.e., 25% of V_w). There will also be induced velocity effects caused by flow deceleration near the rotor disk resulting in a loss of total head (assuming the turbine is extracting energy from the wind). When the turbine is yawed, there will be a skewed wake effects (see Hansen and Xudong[4]). This effect is caused by the fact that the rotation axis of the turbine and the wind are not parallel. The vortex wake produced by the blades must still be convected in the direction of the wind. The vortex wake will then be skewed with respect to the rotor disk. The sum of these induced velocity and skewed wake effects was estimated at approximately 2% of maximum wind velocities. Additional effects caused by vortex wake of the preceding blade (downwash) are not included. The relatively low tip speeds of this turbine coupled with the spacing between the blades, however, suggests that these effects are small.

For nonzero yaw cases, variations in local wind speed resulting in variations in local dynamic pressure q will be affected as well.

Similar to local sinusoidal variations in α, local q values will also vary sinusoidally but maximum q values will be 180-deg out of phase with respect to maximum α. This sinusoidal variation in total velocity (V_{tot}) results in an accelerated flow effect that can be expressed as

$$a = \frac{\mathrm{d}V_{\text{tot}}}{\mathrm{d}t} = \frac{\mathrm{d}\psi}{\mathrm{d}t}\frac{\mathrm{d}V_{\text{tot}}}{\mathrm{d}\psi} = -7.54 V_r V_c \sin\psi / V_{\text{tot}}$$

For $\gamma = 30$ deg and $V_w = 15$ m/s, the relative flow acceleration may be significant. At 30% span, maximum acceleration magnitude is 34.26 m/s^2 or 3.5 g, where g is the sea-level gravitational force. At 80% span, maximum flow acceleration is 5.2 g.

In Rosenhead,[22] Lighthill summarized the effects of flow acceleration in terms of pressure gradient. Positive flow acceleration produces a favorable pressure gradient that can assist in maintaining attached flow and delaying separation. Conversely, negative acceleration produces an adverse pressure gradient that may hasten boundary-layer separation. It was shown in α and q data that positive flow acceleration occurs as the effective α of the blade is decreasing and negative flow acceleration as the effective α of the blade is decreasing and negative flow acceleration as the effective α is increasing. This may result in earlier flow separation and delayed flow separation (or earlier flow reattachment if the flow is separated), respectively, during the rotation cycle and must be taken into account when comparisons with wind tunnel data are made.

Unsteady Aerodynamics

For low blade pitch angles and/or low wind speeds, the effects summarized in the preceding section are sufficient to estimate the quasisteady performance of the wind turbine with sufficient accuracy. To function at peak efficiency, the turbine blade must operate as close to static stall without exceeding the static stall angle. This operational regime provides conditions that are amenable to dynamic stall. Another condition is that the nondimensional fluctuations in effective angle of attack are large as well. Unlike helicopter rotors that run at high tip speeds relative to the freestream, wind turbines operate at relatively low tip speeds. The tip speed for this experiment was approximately 38 m/s, which is two to four times typical wind velocities. Consequently, rapid changes in the inflow, such as sudden wind gusts, can result in sudden increases in effective blade angles of attack even for zero yaw. Changes in wind direction resulting in a yawed disk were seen to result in considerable angle-of-attack variations (Fig. 14). For normal operating conditions, steady-state assumptions are insufficient to predict structural loading and power output, thus requiring analysis of the unsteady flowfields.

A great deal of information regarding unsteady separated flows and dynamic stall phenomena currently exists in the literature.[13–20] Wind-tunnel tests have been conducted for pitching and oscillating wings in constant freestream velocity using qualitative (flow visualization) and quantitative (pressure and force) diagnostic methods. These dynamic variations in α are qualitatively similar to those seen on wind turbine blades where impulsive or cyclic variations in relative wind velocity produce geometrically similar effects. The tower wake was confined to a limited region of the total blade path. As the blade entered the wake, reduced wake velocities resulted in decreased angle of attack. As the blade passed out of the wake, flow velocities increased, resulting in increased angle of attack. This may then be modeled as a single pitch down then pitch up motion. To provide a comparative base, nondimensional pitch rates α^+ were computed to estimate the effective magnitude of the pitch motion. For the zero-yaw case and $V_w = 14.7$ m/s, $\alpha^+ = 0.287$. Over the range of wind velocities examined, α^+ generally varied between 0.15 and 0.3 over the blade span.

The yawed turbine blade was compared with a sinusoidally oscillating wing. Reduced frequency K, mean angle of attack, and oscillation amplitude have been used in wind-tunnel tests to describe differing flow phenomena in terms of these independent variables. Figure 14 demonstrated the significant angle-of-attack variation for a yawed turbine. Reduced frequency was computed based on the velocity normal to the rotor disk and blade rotation frequency. It was found to vary between 0.05 and 0.09, depending on wind velocity and span location.

Helin and Walker[17] investigated the unsteady flowfields and resultant pressure distributions produced by a rectangular wing undergoing a single pitch motion. Robinson[18] characterized dynamic stall vortex formation for sinusoidally oscillating airfoils. Both studies found that a necessary condition for vortex formation is the airfoil to dynamically exceed the static stall angle. Because wind turbines operate near stall, this first and most important criterion is met. Assuming that dynamic stall takes place, the aforementioned studies describe the process as follows: As the airfoil initially exceeds the static stall angle, a separation region forms near the leading edge characterized by high vorticity. As the airfoil continues to pitch up, this region coalesces in the form of a vortex that then proceeds to grow. This vortex is then convected over the airfoil upper surface as it becomes larger and is exposed to the freestream. This vortex is then shed into the wake and is followed by the generation of a trailing-edge vortex, which rotates in a direction opposite that of the dynamic stall vortex. Differing parameters (i.e., α^+, K, and maximum and minimum pitch angle) affect the temporal development of vortex formation as well as the strength of the vortex. These fundamental processes remain intact, however.

Robinson et al.[19] also examined upper surface pressure distributions for a single pitch airfoil to demonstrate the effects of the dynamic stall vortex on the surface pressure. These pressure distributions are remarkably similar to some of the pressure distributions presented in this article. A buildup of LE suction pressure was observed and correlated with attached flow as the wing pitched up. Maximum LE suction pressure occurred during initial formation of the dynamic stall vortex. As this vortex was convected over the upper surface, there was a direct correlation between vortex convection and the location of the suction pressure peak in the upper surface pressure distribution. As the vortex was advected to the aft portion of the wing, integrated normal force data continued to reveal enhanced lift albeit somewhat diminished compared with maximum values. In addition, a strong negative (pitch down) moment was observed even though enhanced lift was maintained. As the vortex was shed into the wake, constant pressure coefficients of -1.0 were observed over the entire upper surface. Similar comparisons have been done for oscillating airfoils (i.e., Refs. 13–15) with similar results. These pressure imprints in the chordwise pressure distribution are generally used to validate the existence and/or quantify the characteristics of a cohesive vortex structure.

The present results are thoroughly consistent with the generation of vortex structures characteristic of dynamic stall. Upper-surface topological pressure distributions (Figs. 6, 8, and 9) showed dominant pressure rises. In addition, chordwise pressure distributions taken at individual points in the rotation cycle (Figs. 10 and 11) demonstrated definite suction pressure peaks. These pressure peaks moved downstream as the cycle advanced, indicating convection of a vortex structure. The most convincing evidence may be found in the normal force data and corresponding moment data (Figs. 12 and 13). Even as the airfoil section was generating considerable lift in excess of maximum steady-state values, a strong negative pitch moment was observed. This negative pitching moment would not exist if the flow was attached. If the flow was completely separated, the high normal forces would not be seen. The remaining explanation lies in the formation of a dynamic stall vortex.

Correlation of pressure, normal force, and moment data substantiate claims of dynamic stall on wind turbines. This is most clearly seen for the 30-deg yaw case at 30% span. At $\psi = 186$ deg, maximum LE pressure was attained and the moment coefficient indicated attached flow. Normal force coefficient is still rising, however. By $\psi = 196$ deg, the suction pressure peak has moved to 12.5% c. Normal force coefficient is rising but moment coefficient remains constant at -0.12. By $\psi = 227$ deg, the suction pressure peak has moved to approximately 40% c and normal force has reached its maximum. Because of movement of the suction pressure peak, negative pitching moment reached a maximum, normal force begins to decrease and the suction pressure peak has translated to approximately 65% c. Trends seen in these data are similar to trends seen in Refs. 17 and 19, where additional visualization of a dynamic stall vortex was correlated with pressure, normal force, and moment data.

Data for the 30-deg yaw case at 63% span demonstrated a somewhat different flow development. At $\psi = 276$ deg, the maximum LE pressure was seen. Correlation with moment data suggests attached flow. The normal force coefficient remains approximately constant. By $\psi = 284$ deg, the suction pressure peak has moved to 18% c. Moment coefficient is just beginning to increase, and normal force coefficient just begins to decrease. By $\psi = 290$ deg, peak moment coefficient was seen but there was no evidence of a suction pressure peak. These data suggest that a dynamic stall vortex forms but detaches from the surface by the time it reaches 20% c. Normal force and moment coefficient data are then indicative of separated flow conditions.

If and when dynamic stall occurs, it may not occur along the entire blade and may not occur at the same point in the rotational cycle. Indeed, the present experimental evidence suggests that dynamic stall occurred at later times for outboard spanwise locations and the severity of the stall was diminished. For the 30-deg yaw case, vortex formation was first seen at $\psi = 192$ deg at 30% span, $\psi = 228$ deg at 47% span, and $\psi = 276$ deg at 63% span. At 80% span, there was no evidence of dynamic stall vortex formation.

This trend is explained by the variation in angle of attack over the rotation cycle for each of the span locations. Because the blade is untwisted, the angle of attack is a function of wind geometry alone. Local angle of attack vs ψ (Fig. 14) showed α variations between 14 and 66 deg at 30% span, 8 and 41 deg at 47% span, 6 and 26 deg at 63% span, and 2 and 16 deg at 80% span. As was mentioned earlier, a necessary condition for dynamic stall vortex formation is to dynamically exceed the static stall angle. In addition, as the stall angle is exceeded to a larger degree, the vortex that forms would be expected to be larger and more energetic. At 30 and 47% span, minimum α was below the static stall angle, and the dynamic pitch angle increased significantly beyond the static stall angle. The greatest evidence of vortex formation was seen at these two locations. At 63% span, maximum α was only 26 deg. Pressure and moment data implied a weaker vortex structure. At 80% span, maximum α was equivalent to the static stall angle. Because static stall was not exceeded, a cohesive vortex structure was not produced, but enhanced lift values were observed. It is possible that this may be a result of the influence of the large-scale structures produced inboard.

This temporal shifting of dynamic stall to different blade span locations may be desirable for engineering purposes. Because dynamic stall occurs at different points over the rotation cycle for differing span locations, the large transient loading experienced by the blade as a whole may be smeared over a greater portion of the rotation cycle. By adding twist to the blade, blade designers hope to maintain equivalent angles of attack over the entire blade span. Sudden wind gusts or changes in wind direction may cause the entire blade to experience dynamic stall instead of just a portion of it. This aspect needs to be considered in the wind turbine design process.

As the blade passes through the tower wake, different flow development was observed that may or may not result in dynamic stall vortex formation. Reasons for this include a much shorter duration of the event and diminished magnitudes in terms of pressures and forces. Data taken at 80% span for the different wind speeds, however, clearly demonstrated lift overshoots at the higher wind speeds for cases where local angle of attack was above the static stall angle. For zero yaw and $V_w = 23$ m/s, local blade angle of attack was approximately 25 deg. As the blade entered the wake, α decreased and reached a minimum of 15 deg, which was just below the static stall angle. As the blade exited the tower wake, the local angle of attack then increased back to 25 deg. It is likely that as the blade entered the wake, the flowfield reattached. As local α increased, the flow remained attached. The enhanced lift may or may not have resulted from a dynamic stall vortex. It is possible that the lift overshoot was caused by delayed separation or a momentarily energized boundary layer. Even so, angle of attack variations along the blade are between 5 and 10 deg, depending on span location and wind velocity. This value is small compared with the α variations produced by nonzero-yaw angles. The effect of the tower wake is felt along the entire blade at the same time in the rotation cycle, however, and does result in an impulsive force along the entire blade with a 50-Hz duration. Although not shown, this does excite the blade's resonant frequencies.

Conclusions

A joint research effort between the National Renewable Energy Laboratory and the University of Colorado has resulted in the systematic analysis of select data sets from a downstream HAWT operating in a field environment. These data clearly demonstrate the aerodynamic complexities associated with a wind turbine blade for the most basic operating conditions. Definite unsteady and three-dimensional behavior have been presented and discussed, with a focus on the dynamic stall process. An overview of the wind turbine operating states and the unsteady aerodynamics were provided.

Under conditions where wind velocity and yaw were constant, significant lift enhancement was routinely observed. For limiting test cases, they were observed even at outboard span locations where a majority of the force is produced. Normal force values as great as two times maximum steady-state values were routinely observed from 30 to 63% span locations. These enhanced lift values were shown to be a result of dynamic stall vortex formation. Although dynamic stall was not seen to occur at 80% span, enhanced lift values were still observed possibly because of the influence of the structures produced inboard. Regardless, the results exhibited complex temporal and spatial three-dimensional behavior. Dynamic stall was seen to occur at later times in the rotational cycle at outboard span locations spreading out the large transient forces over the entire blade.

Analytic models of angle of attack and local dynamic pressure were formulated based on the geometry of the wind turbine and incoming flowfield. Experimental data confirmed the validity of the geometric model used in this article, although an improved tower wake model must still be constructed.

The work presented in this article only begins to address many issues concerning forced unsteady separated flowfields that are produced by HAWT. Under normal operating conditions, the geometry of the turbine relative to the wind is constantly changing. Future studies that address the dynamic variations in yaw as well as effects of dynamic blade oscillations will need to be conducted. Care must also be taken when designing twisted blades because they may make the undesirable effects of dynamic stall even worse. The Combined Experiment provided a wealth of experimental data that can be used to identify current and potential problems to the wind turbine industry. Recognizing this potential may assist in developing future cooperative research projects both inside and outside of the wind turbine industry.

Acknowledgments

Funding for this research was provided by the U.S. Department of Energy through Contract DE-AC36-83CH10093. The principal author conducted this research at the National Renewable Energy Laboratory under a postdoctoral fellowship program sponsored by Associated Western Universities, Inc.

References

[1] Butterfield, C. P., "Three-Dimensional Airfoil Performance Measurements on a Rotating Wing," Solar Energy Research Inst., SERI/TP-217-3505, Golden, CO, June 1989.

[2] Butterfield, C. P., Jenks, M., Simms, D. A., and Musial, W. P., "Aerodynamic Pressure Measurements on a Rotating Wind Turbine Blade," Solar Energy Research Inst., SERI/TP-257-3695, Golden, CO, May 1990.

[3] Butterfield, C. P., Scott, G., and Musial, W. P., "Comparison of Wind Tunnel Airfoil Performance Data with Wind Turbine Blade Data," Solar Energy Research Inst., SERI/TP-254-3799, Golden, CO, July 1990.

[4] Hansen, A. C., and Xudong, C., "Yaw Dynamics of Horizontal Axis Wind Turbines," Solar Energy Research Inst., SERI/STR-217-3476, Golden, CO, March 1989.

[5] Butterfield, C. P., Hansen, A. C., Simms, D. A., and Scott, G., "Dynamic Stall on Wind Turbine Blades," *AWEA Windpower '91 Conference Proceedings*, Palm Springs, CA, 1991.

[6] Hansen, A. C., and Butterfield, C. P., "Aerodynamics of Horizontal Axis Wind Turbines," *Annual Review of Fluid Mechanics*, Vol. 25, March 1993, pp. 115–149.

[7] Huyer, S. A., "Examination of Forced Unsteady Separated Flow Fields on a Rotating Wind Turbine Blade," National Renewable Energy Lab., NREL/TP-442-4864, Golden, CO, April 1993.

[8] Butterfield, C. P., Musial, W. P., and Simms, D. A., "Combined Experiment Phase I Final Report," National Renewable Energy Lab., NREL/TP-257-4655, Golden, CO, Oct. 1992.

[9] McNiff, B., and Simms, D. A., "Error Analysis in Wind Turbine Field Testing," *Windpower '92 Proceedings* (Seattle, WA), American Wind Energy Association, Washington, DC, 1992.

[10] Butterfield, C. P., Jenks, M., Simms, D. A., and Musial, W. P., "Aerodynamic Pressure Measurements on a Rotating Wind Turbine Blade," *Proceedings of the 36th International Instrumentation Symposium* (Denver, CO), Instrument Society of America, Research Triangle Park, NC, 1990, pp. 517–524.

[11] Simms, D. A., and Butterfield, C. P., "A PC-Based Telemetry System for Acquiring and Reducing Data from Multiple PCM Streams," *Proceedings of the International Telemetering Conference* (Las Vegas, NV), Vol. 27, International Foundation for Telemetering, Woodland Hills, CA, 1991, pp. 189–199.

[12] Spera, D. A., *Wind Turbine Technology: Fundamental Concepts of Wind Turbine Engineering*, American Society of Mechanical Engineers Press, New York, 1994.

[13] McCroskey, W. J., Carr, L. W., and McAlister, K. W., "Dynamic Stall Experiments on Oscillating Airfoils," AIAA Paper 75-125, Jan. 1975.

[14] McCroskey, W. J., "Unsteady Airfoils," *Annual Review of Fluid Mechanics*, Vol. 14, 1982, pp. 285–311.

[15] Carr, L. W., McAlister, K. W., and McCroskey, W. J., "Analysis of the Development of Dynamic Stall Based on Oscillating Airfoil Experiments," NASA TN D-8382, Jan. 1977.

[16] Huyer, S. A., Reavis, M. A., and Luttges, M. W., "A Comparative Study of Differing Vortex Structures Arising in Unsteady Separated Flows," *Proceedings of the AIAA 6th Applied Aerodynamics Conference* (Williamsburg, VA), AIAA, Washington, DC, 1988, pp. 483–491 (AIAA Paper 88-2582).

[17] Helin, H. E., and Walker, J. M., "Interrelated Effects of Pitch Rate and Pivot Point on Airfoil Dynamic Stall," AIAA Paper 85-0130, Jan. 1985.

[18] Robinson, M. C., "Development of Vorticity and Vortices from Forced Unsteady Flow Separation," Ph.D. Thesis, Dept. of Aerospace Engineering Studies, Univ. of Colorado, Boulder, CO, 1985.

[19] Robinson, M. C., Walker, J., and Wissler, J., "Unsteady Surface Pressure Measurements on a Pitching Rectangular Wing," *Workshop II on Unsteady Separated Flows*, U.S. Air Force Academy, FJSRL-TR-88-0004, Colorado Springs, CO, 1987, pp. 225–237.

[20] Freymuth, P., "Visualizing the Connectivity of Vortex Systems for Pitching Wings," *1st National Congress of Fluid Dynamics*, Cincinnati, OH, 1985.

[21] Schlichting, H., *Boundary Layer Theory*, 6th ed., McGraw–Hill, New York, 1968.

[22] Rosenhead, L., *Laminar Boundary Layers*, Dover, New York, 1963.